Spatial distribution of a depletion potential between a big solute of arbitrary geometry and a big sphere immersed in small spheres

Masahiro Kinoshita
Institute of Advanced Energy, Kyoto University, Uji, Kyoto 611-0011, Japan

(Received 15 October 2001; accepted 28 November 2001)

The hypernetted-chain integral equations are solved on a three-dimensional cubic grid to calculate the spatial distribution of the depletion potential between a big solute of *arbitrary geometry* and a big sphere immersed in small spheres forming the solvent. By analyzing the potential along a specific trajectory of the big sphere, effects due to the geometric feature of the big solute (step edges, trenches, corners, changing curvature, etc.) can be examined in detail. As an illustration, effects of the step edge on the lateral depletion potential along a wall surface are analyzed. Along the trajectory considered, the big sphere moves at constant height, starting on the center of the wall surface and moving horizontally past the edge. The big sphere is repelled from the edge into the wall surface, and to escape to the bulk it must overcome a significantly high free-energy barrier. As another illustration, simple model calculations are performed for the *lock and key* steric interaction between macromolecules. The potential at contact (i.e., the stabilization free energy) for the key that exactly fits the lock is far larger than for smaller and larger keys and considerably in excess of the value predicted by the Asakura–Oosawa theory. © *2002 American Institute of Physics.*
[DOI: 10.1063/1.1445106]

I. INTRODUCTION

In a colloidal suspension containing particles of two significantly different sizes, where the number density of smaller particles is much higher than that of larger ones, an attractive force is induced between the larger particles at small separations. This is due to the extra volume that becomes available to the smaller particles when the larger particles approach each other and the excluded regions (i.e., regions from which the smaller particles are excluded) overlap, thus increasing the system entropy. The gain in entropy becomes even greater when the larger particle moves to a flat wall. These entropic excluded-volume (depletion) effects are known to cause phase separation phenomena in the bulk and at flat surfaces.[1,2] Furthermore, the shape of the wall can lead to entropic forces in a specific direction *along the wall*. For example, it was experimentally demonstrated that the larger particles are locally repelled from a step edge into the wall.[3] If the wall has constantly changing radius of curvature, the forces act everywhere along it. Manipulation techniques based on these depletion effects are expected to be useful for making highly ordered particle arrays.

The depletion effects should play crucial roles in biological systems[4–6] as well. Many biological processes are controlled by the interactions between macromolecules and by those of macromolecules with cell membranes. The macromolecules and membranes generate excluded volumes for the smaller particles forming the solvent, giving rise to the depletion forces contributing to the interactions to a great extent. From a physical viewpoint, it is interesting to study the depletion effects *exclusively* by employing simplified models combined with theoretical methods or computer simulations. In such studies, the solvent particles, macromolecules, and membranes can be modeled as small hard spheres, big hard bodies, and hard walls, respectively. Notice, however, that geometric features of the hard bodies and wall surfaces are very important factors to be accounted for in the studies. For example, variation of the local curvature of the wall surface creates depletion forces in a specific direction *along the surface*, that is, the *lateral* depletion forces. Further, the depletion forces between big bodies with arbitrary shapes must be substantially different from those between big spheres.

A theoretical argument was first given by Asakura and Oosawa,[7] and afterwards a variety of more advanced theories has been developed and applied to analyses of the depletion effects. Computer simulations have also been performed rather extensively. Nevertheless, these studies are limited to the interactions between two big spheres (convex surfaces) and between a big sphere and a flat wall.[8–13] As the only exception, Roth *et al.*[14] calculated the interaction between a concave surface and a big sphere using the density functional theory[15] (DFT). They calculated the depletion potentials between a big sphere and convex and concave surfaces having various curvatures and suggested that a lateral depletion force along a surface with changing curvature be approximately estimated from these potentials. Very recently, Roth *et al.*[16] developed a versatile DFT approach for calculating the depletion potentials. It is potentially applicable to a solute of arbitrary geometry, but it has been illustrated only for a big sphere and a flat wall.

A powerful tool for going beyond the well-studied solutes of simple geometry (i.e., spheres and flat walls) is the hypernetted-chain (HNC) integral equation theory. The results from the HNC theory are not very accurate because the bridge functions are neglected. However, it has been verified that the HNC theory gives quantitatively reliable results for

the interactions between big spheres immersed in small spheres, for diameter ratios as small as 0.033, and for packing fractions of the small spheres as high as 0.383 (see Figs. 1 and 4 of Ref. 17). In the present article, the author employs the HNC integral equations solved on a three-dimensional (3D) discrete cubic grid[18,19] to calculate the spatial distribution of the depletion potential between a big solute of *arbitrary geometry* and a big sphere immersed in small spheres forming the solvent.[20] In the usual HNC theory for spherical particles, the results can be made very accurate by including appropriate bridge functions.[9,13] In the present case where a solute of arbitrary geometry is treated, on the other hand, such an inclusion cannot readily be achieved yet. However, a quantitative examination of the results from the 3D-HNC approach is performed below, proving that the approach is reliable enough to draw significant conclusions on the depletion effects.

Once the spatial distribution of the depletion potential is calculated, by analyzing the potential along a specific trajectory of the big sphere, effects due to the geometric feature of the big solute (step edges, trenches, corners, changing curvature, etc.) can be examined in detail. As an illustration, effects of the step edge on the lateral depletion forces are calculated and shown to be in reasonable agreement with a recent experimental observation.[3] Effects of a trench are also briefly studied. As another illustration, simple model calculations are performed for the *lock and key* steric interaction between macromolecules, and it is shown that the depletion effects provide the interaction with remarkably high selectivity. That is, even when some keys of different sizes coexist, the key that exactly fits the lock is *exclusively* stabilized by the contact. In earlier works performed for the potentials between big spheres[8,14] and between a big sphere and a flat wall,[13] it was suggested that the Asakura–Oosawa (AO) theory was accurate for the potential at contact despite its simplicity. However, this is not always true in cases of more complicated geometry considered in the present model calculations, and the selectively given is much higher than one might expect from the overlap of the excluded regions and the AO theory. In the two illustrations, the depletion forces are analyzed and discussed in detail by relating them to the packing effects of the small spheres.

II. MODEL AND THEORY

It is assumed that a solute i of arbitrary geometry is immersed in solvent at infinite dilution. The Ornstein–Zernike equation in the Fourier space is expressed by

$$W_{is}(k_x,k_y,k_z)=\rho_s C_{is}(k_x,k_y,k_z)H_{ss}(k), \tag{1}$$

and the HNC closure equation is written as

$$c_{is}(x,y,z)=\exp\{-u_{is}(x,y,z)/(k_BT)\}\exp\{w_{is}(x,y,z)\}-w_{is}(x,y,z)-1. \tag{2}$$

Here, the subscript s denotes the solvent, c is the direct correlation function, h the total correlation function, $w=h-c$, u the potential, ρ the number density, and k_BT Boltzmann's constant times the absolute temperature. The capital letters (C, H, and W) represent the Fourier transforms. $H_{ss}(k)$ ($k^2=k_x^2+k_y^2+k_z^2$) calculated using the usual HNC theory for spherical particles is part of the input data. The numerical procedure is briefly summarized as follows: (1) $u_{is}(x,y,z)$ is calculated at each 3D grid point, (2) $w_{is}(x,y,z)$ is initialized to zero, (3) $c_{is}(x,y,z)$ is calculated using Eq. (2), (4) $c_{is}(x,y,z)$ is transformed to $C_{is}(k_x,k_y,k_z)$ using the 3D fast Fourier transform (3D-FFT), (5) $W_{is}(k_x,k_y,k_z)$ is calculated from Eq. (1), (6) $W_{is}(k_x,k_y,k_z)$ is inverted to $w_{is}(x,y,z)$ using the 3D-FFT, and (7) steps (3)–(6) are repeated until the input and output functions become identical within convergence tolerance.

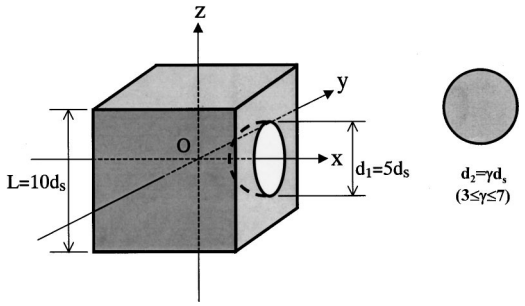

FIG. 1. Model solutes considered. Solute 1 is a hard cube having a hemispherical cavity with diameter d_1, and the length of a step edge is L. Solute 2 is a big hard sphere with diameter d_2. These solutes are immersed in small hard spheres with diameter d_s at infinite dilution. L and d_1 are set at $10d_s$ and $5d_s$, respectively. Three different values, $4d_s$, $5d_s$, and $6d_s$, are mainly considered for d_2, but $3d_s$ or $7d_s$ is also tested. The coordinate system is chosen such that the origin is at the center of the cube.

Unless otherwise specified, the author considers solute 1 and solute 2 immersed in small spheres forming the solvent (the bulk density is ρ_s), which are illustrated in Fig. 1. Solute 1 is a hard cube with a hemispherical cavity and solute 2 is a big hard sphere. The author tests three different diameters of the big sphere that are smaller than, equal to, and larger than the diameter of the cavity, respectively. First, the solute-1–solvent correlation functions are calculated by following the procedure described above ($i=1$). On grid points where the solvent particle and solute 1 overlap, $\exp\{-u_{is}(x,y,z)/(k_BT)\}$ is zero. On those where the solvent particle is at contact with solute 1, it is set at 0.5, and otherwise it is unity. Second, the solute-2–solvent correlation functions [the Fourier transform of the total correlation function is denoted by $H_{2s}(k)$] are calculated using the usual HNC theory for spherical particles. The potential of mean force between the two solutes $\Phi_{12}(x,y,z)$ is then obtained from

$$\Phi_{12}(x,y,z)/(k_BT)=u_{12}(x,y,z)/(k_BT)-w_{12}(x,y,z), \tag{3}$$

where $w_{12}(x,y,z)$ is calculated by inverting $W_{12}(k_x,k_y,k_z)$ given by

$$W_{12}(k_x,k_y,k_z)=\rho_s C_{1s}(k_x,k_y,k_z)H_{2s}(k). \tag{4}$$

The grid spacing (Δx, Δy, and Δz) is set at $0.1d_s$, and the grid resolution ($N_x\times N_y\times N_z$) is $256\times256\times256$. It has been verified that the spacing is sufficiently small and the box size ($N_x\Delta x$, $N_y\Delta y$, and $N_z\Delta z$) is large enough. Taking the lock–key interaction as an example, effects of the grid spacing on

TABLE I. Effects of the grid spacing on the stabilization free energy (SFE) calculated. SFE is the value of the lock–key depletion potential at contact. $L=5d_s$ and $d_1=3d_s$ are also tested with $d_2=2d_s$, $3d_s$, and $4d_s$.

L	d_1	d_2	$N_x=N_y=N_z$	$\Delta x=\Delta y=\Delta z$	SFE
$5d_s$	$3d_s$	$2d_s$	64	$0.2d_s$	−10.8
			128	$0.1d_s$	−9.84
			256	$0.05d_s$	−9.82
$5d_s$	$3d_s$	$3d_s$	64	$0.2d_s$	−49.9
			128	$0.1d_s$	−49.3
			256	$0.05d_s$	−49.4
$5d_s$	$3d_s$	$4d_s$	64	$0.2d_s$	−11.4
			128	$0.1d_s$	−11.6
			256	$0.05d_s$	−11.7
$10d_s$	$5d_s$	$4d_s$	128	$0.2d_s$	−33.5
			256	$0.1d_s$	−33.6
$10d_s$	$5d_s$	$5d_s$	128	$0.2d_s$	−132
			256	$0.1d_s$	−129
$10d_s$	$5d_s$	$6d_s$	128	$0.2d_s$	−21.2
			256	$0.1d_s$	−19.5

the numerical accuracy are illustrated in Table I where the stabilization free energy (see Sec. III D) is chosen as a representative parameter.

III. RESULTS AND DISCUSSION

A. Depletion potential between a big sphere and a flat wall

With a sufficiently large value of L, $\Phi_{12}(x,0,0)$ for $x \leqslant -(L+d_2)/2$ can be regarded as a depletion potential between a big sphere and a flat wall, $\Phi_{\text{wall}}(h)$ (h is the surface separation), which has already been studied extensively. The author compares the DFT results from Ref. 16 with those from the 3D-HNC approach in Fig. 2 ($d_2/d_s=5$ and $\eta_s=\pi\rho_s d_s^3/6=0.1$, 0.2, and 0.3). The DFT results are reportedly in good agreement with the computer simulation data from Ref. 13 and can be regarded as almost exact ones. The 3D-HNC approach reproduces the detailed structure of the potential and gives reasonable agreement with the DFT results.

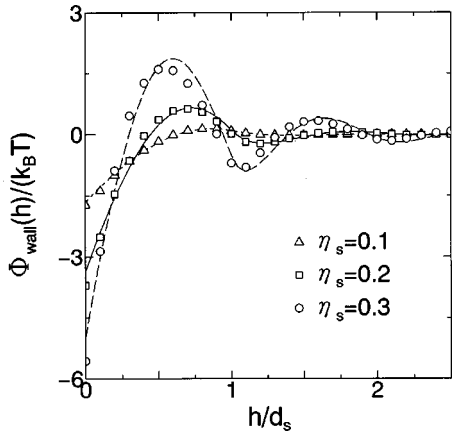

FIG. 2. Comparison between the DFT results (Ref. 16) (dotted, solid, and broken lines) and those from the 3D-HNC approach in terms of the depletion potential $\Phi_{\text{wall}}(h)$ between a big sphere ($d_2/d_s=5$) and a flat wall for three different values of the packing fraction of the small spheres η_s. In the 3D-HNC approach, solute 1 shown in Fig. 1 is treated. The surface separation is denoted by h. The potential is scaled by k_BT.

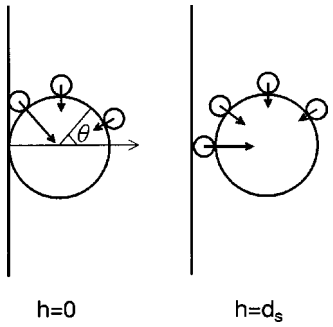

FIG. 3. Forces acting on a big sphere at or near contact with a flat wall. Forces originating from the contact density are represented by the arrows. A longer arrow corresponds to a stronger force.

It tends to overestimate the potential at contact, but the errors are only ~4.5%, ~9.9%, and ~11% for $\eta_s=0.1$, 0.2, and 0.3, respectively. The author denotes the reduced density profile of the small spheres by $g(x,y,z)$ $[=h_{1s}(x,y,z)+1]$. The number of the small spheres within the infinitesimal volume $dxdydz$ is given by $\rho_s g(x,y,z)dxdydz$. With a sufficiently large value of L, $g(x,0,0)$ for $x \leqslant -(L+d_s)/2$ can be regarded as a reduced density profile near a flat wall. Our value at contact $g(-(L+d_s)/2,0,0)$ is larger than the exact value from the contact theorem,[13] but the errors are only ~3.8%, ~11%, ~14%, and ~14% for $\eta_s=0.1$, 0.2, 0.3, and 0.367, respectively. Notice, however, that $L=10d_s=2d_2$ may not be sufficiently large. A significantly larger value of L (e.g., $20d_s=4d_2$) would lead to better agreement, but it is not easy to test, because due to a much larger box size the amount of computer storage requirements becomes unacceptably large on our workstation. In summary, the reduced density profile and the depletion potential calculated using the 3D-HNC approach are both quantitatively reliable. They are not very accurate, but the conclusions drawn are not likely to be altered.

A physical explanation of the depletion potential in dense small spheres can be given by looking at the depletion force $-d\Phi_{\text{wall}}(h)/dh$. The force can be discussed in terms of the density of the small spheres at contact around the big sphere.[8,13] At a big sphere and a flat wall the contact density is considerably in excess of ρ_s. When the big sphere is at or near contact with the flat wall, an additional, important factor arises: *The contact density is further enhanced in the vicinity of the corner or channel confined between the two surfaces.* Choosing the big-sphere center as the origin and using polar coordinates, the author expresses the contact density as $\rho_c(r=(d_2+d_s)/2,\theta)$ (θ is measured from the positive axis normal to the flat surface; see Fig. 3). Forces originating from ρ_c for $0 \leqslant \theta < \pi/2$ and from ρ_c for $\pi/2 < \theta \leqslant \pi$ (ρ_c is symmetrical about $\theta=\pi$), respectively, constitute attractive and repulsive components of the net force. At $h=d_s$, ρ_c increases as θ approaches π and the net force is repulsive. At $h=0$, ρ_c for $\pi/2 < \theta \leqslant \theta_{\max}$ makes a significantly large, repulsive contribution but ρ_c vanishes for $\theta_{\max} < \theta \leqslant \pi$ where $\cos\theta_{\max}=-(d_2-d_s)/(d_2+d_s)$, leading to an attractive net force. The net force vanishes at a surface separation smaller than d_s. The attractive and repulsive components are large but comparable in magnitude, and the net force becomes

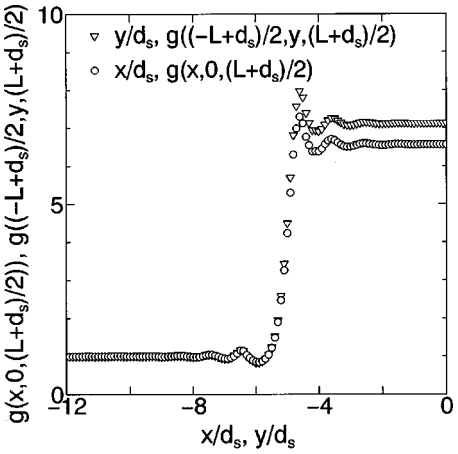

FIG. 4. The reduced density profiles of the small spheres, $g(x,0,(L+d_s)/2)$ and $g((-L+d_s)/2,y,(L+d_s)/2)$. Solute 1 is treated. Since they are almost exactly symmetrical about $x=0$ and $y=0$, respectively, the profiles are shown only for $x\leqslant 0$ and $y\leqslant 0$. The step edge is located at $x=-L/2$ and $y=-L/2$ ($x/d_s=-5$ and $y/d_s=-5$), respectively.

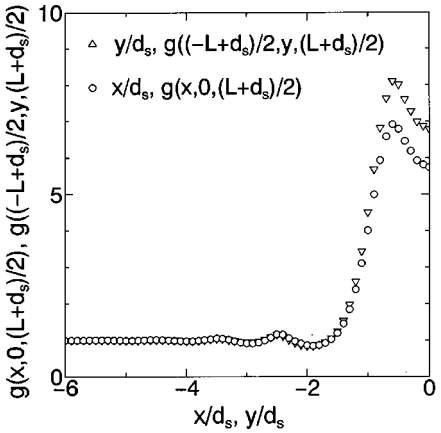

FIG. 5. The reduced density profiles of the small spheres, $g(x,0,(L+d_s)/2)$ and $g((-L+d_s)/2,y,(L+d_s)/2)$. A hard cube ($L=2d_s$) without the cavity is considered as the solute. Since they are exactly symmetrical about $x=0$ and $y=0$, respectively, the profiles are shown only for $x\leqslant 0$ and $y\leqslant 0$. The step edge is located at $x/d_s=-1$ and $y/d_s=-1$, respectively.

considerably smaller. In the AO theory where nonzero ρ_c is set equal to ρ_s, for $0\leqslant h\leqslant d_s$ the attractive component is remarkably underestimated but the repulsive one is underestimated *even more*. The AO theory benefits from this fortuitous cancellation of errors and the net force calculated (a purely attractive force with a range of one small-sphere diameter) does not depart seriously from the exact one. Moreover, at $h=d_s$ the AO force is zero while the exact one is repulsive, and at $h=0$ the former is attractive but weaker than the latter (see Fig. 3 of Ref. 13). As a result, the potential at contact, which is obtained by integrating the net force over the surface separation, can be predicted by the theory with sufficiently high accuracy. This is not always true, however, in cases of more complicated geometry considered in the present study (see below).

B. Two-dimensional packing of small spheres on a square surface

Solute 1 shown in Fig. 1 is treated and η_s is fixed at 0.367. The reduced density profiles of the small spheres, $g(x,0,(L+d_s)/2)$ for $x\leqslant 0$ and $g((-L+d_s)/2,y,(L+d_s)/2)$ for $y\leqslant 0$, are shown in Fig. 4. As the step edge is approached from the bulk, the profiles become more oscillatory. They increase steeply near the edge, taking the highest values at $x\sim(-L+d_s)/2$ and $y\sim(-L+d_s)/2$ on the wall surface, respectively. They become less oscillatory as the center of the surface is approached. The local maximums of $g(x,y,z)$ occur at $x\sim(-L+d_s)/2\pm nd_s$ and $y\sim(-L+d_s)/2\pm nd_s$ ($n=0,1,...$) and the global maxima at the four locations, $(x,y)\sim((-L+d_s)/2,(-L+d_s)/2)$, $((L-d_s)/2,(-L+d_s)/2)$, $((-L+d_s)/2,(L-d_s)/2)$, and $((L-d_s)/2,(L-d_s)/2)$. These results are indicative of formation of a dense monolayer of the small spheres on the surface, which can be referred to as the *two-dimensional packing* of the small spheres. Along the x axis for $x<0$, for example, a small sphere is stabilized at $x\sim(-L+d_s)/2$ more than at any adjacent locations. At locations deep into the wall surface, on the other hand, they are almost equally stabilized, which is reflected in the flatness of the profile.

It is worthwhile to change L and calculate the reduced density profiles. A hard cube without the cavity is treated with $L=2d_s$ and $2.5d_s$. The profiles $g(x,0,(L+d_s)/2)$ for $x\leqslant 0$ and $g((-L+d_s)/2,y,(L+d_s)/2)$ for $y\leqslant 0$ are shown in Fig. 5 for $L=2d_s$ and in Fig. 6 for $L=2.5d_s$. The step-edge effects observed are larger due to the smaller values of L. Again, the global maxima occur at the four locations, $(x,y)\sim((-L+d_s)/2,(-L+d_s)/2)$, $((L-d_s)/2,(-L+d_s)/2)$, $((-L+d_s)/2,(L-d_s)/2)$, and $((L-d_s)/2,(L-d_s)/2)$. It is interesting to note that the values of $g(x,y,z)$ at the four locations are roughly independent of L and always significantly high. On the center the profiles for $L=2d_s$ take local minimums while those for $L=2.5d_s$ take local maxima. The most stable packing could be depicted as shown in Fig. 7,

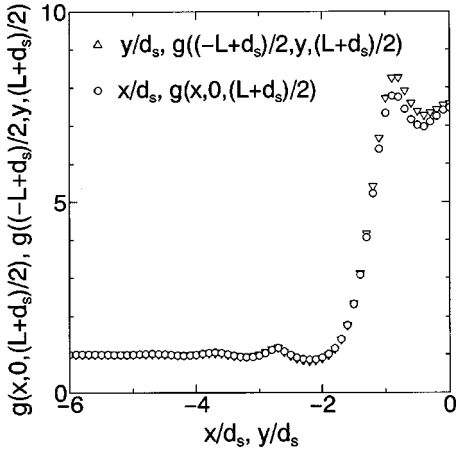

FIG. 6. The reduced density profiles of the small spheres, $g(x,0,(L+d_s)/2)$ and $g((-L+d_s)/2,y,(L+d_s)/2)$. A hard cube ($L=2.5d_s$) without the cavity is considered as the solute. Since they are exactly symmetrical about $x=0$ and $y=0$, respectively, the profiles are shown only for $x\leqslant 0$ and $y\leqslant 0$. The step edge is located at $x/d_s=-1.25$ and $y/d_s=-1.25$, respectively.

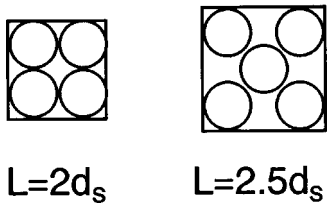

FIG. 7. The most stable packing of the small spheres on a square surface. In the case of $L=2.5d_s$, spheres are placed on the four global-maximum locations, and then one more is placed on the center where it does not overlap the four spheres and the reduced density profile has a local maximum.

indicating that the small spheres are packed as efficiently as possible on the surface.

C. Step-edge effects on lateral depletion potential along a wall surface

The solutes shown in Fig. 1 are treated with $d_2=4d_s$, $5d_s$, $6d_s$, and $7d_s$ and η_s is fixed at 0.367. The depletion potential $\Phi_{12}(x,0,(L+d_2)/2)$ is shown for $x\leqslant 0$ in Fig. 8. There is a shallow minimum located at $x\sim -L/2+\zeta$ (ζ is $\sim 0.9d_s$, $\sim 1.0d_s$, $\sim 1.1d_s$, and $\sim 1.2d_s$ for $d_2=4d_s$, $5d_s$, $6d_s$, and $7d_s$, respectively). The big sphere is repelled *from the edge into the wall surface*. To escape to the bulk, the big sphere must overcome a free-energy barrier, $\Phi_{12}(-L/2-\xi,0,(L+d_2)/2)-\Phi_{12}(-L/2+\zeta,0,(L+d_2)/2)$, taking the values of $\sim 6.3k_BT$, $\sim 7.7k_BT$, $\sim 9.0k_BT$, and $\sim 10k_BT$, respectively. A positive peak occurs near the edge, at $x\sim -L/2-\xi$ (ξ is $\sim 1.3d_s$, $\sim 1.4d_s$, $\sim 1.6d_s$, and $\sim 1.7d_s$, respectively). These results are all in qualitatively good agreement with the experimental observation reported in Ref. 3. Notice that the positive peak exists even in the horizontal trajectory. It is difficult to compare our results *quantitatively* with the experimental data, because the data were averaged over a variety of trajectories. The author just mentions that under the experimental condition, $\eta_s=0.300$ and

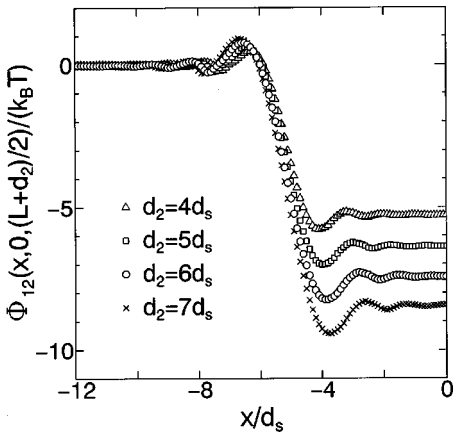

FIG. 8. The depletion potential Φ_{12} between solute 1 and solute 2 (the big sphere) along the trajectory of the big sphere: $x\leqslant 0$, $y=0$, and $z=(L+d_2)/2$. It is scaled by k_BT and plotted for the four different values of d_2, $4d_s$, $5d_s$, $6d_s$, and $7d_s$. Since the potential is almost exactly symmetrical about $x=0$, the curves are shown only for $x\leqslant 0$. The step edge is located at $x=-L/2$ ($x/d_s=-5$). If we assume that the big sphere moves in the negative direction along the x axis, it moves at constant height, starting on the center of the wall surface and moving horizontally past the edge.

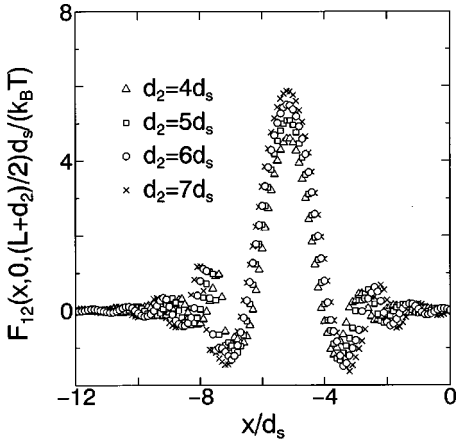

FIG. 9. The depletion force $F_{12}=-\partial\Phi_{12}/\partial x$ between solute 1 and solute 2 (the big sphere) along the trajectory of the big sphere: $x\leqslant 0$, $y=0$, and $z=(L+d_2)/2$. The force is calculated by numerical differentiation of the potential plotted in Fig. 8.

$d_2=5.54d_s$, the free-energy barrier calculated by the 3D-HNC approach is $\sim 6.5k_BT$ while the AO value is $\sim 5.3k_BT$. Since the AO theory can reproduce neither the shallow minimum nor the positive peak, it underestimates the barrier. If the barrier is calculated as $\Phi_{12}(-\infty,0,(L+d_2)/2)-\Phi_{12}(0,0,(L+d_2)/2)$ by neglecting the shallow minimum and the positive peak, the value from the 3D-HNC approach is $\sim 5.8k_BT$, which is fairly close to the AO value. As far as the potential on the wall-surface center is concerned, the AO theory gives a fairly accurate value.

The depletion force $F_{12}(x,0,(L+d_2)/2)=-\partial\Phi_{12}(x,0,(L+d_2)/2)/\partial x$ is calculated by numerical differentiation and plotted in Fig. 9. Let us consider the trajectory of the big sphere moving in the positive direction along the x axis. $\Phi_{12}(x,0,(L+d_2)/2)$ is given by

$$\Phi_{12}(x,0,(L+d_2)/2)=-\int_{-\infty}^{x}F_{12}(x,0,(L+d_2)/2)dx. \quad (5)$$

Choosing the big-sphere center as the origin, the author expresses the contact density as $\rho_c(r=(d_2+d_s)/2,\theta)$, where θ is measured from the positive z axis. Forces arising from ρ_c for $0<\theta<\pi$ and from ρ_c for $\pi<\theta<2\pi$ (ρ_c is *not symmetrical* about $\theta=\pi$), respectively, constitute positive (i.e., the sphere is pulled in the positive direction along the trajectory considered) and negative components of the net force. The force curve takes a negative, local-minimum value at $x\sim x_q=(-L+d_s)/2-(d_2d_s)^{1/2}$ that corresponds to the position where the big sphere touches the small sphere located at $x\sim(-L+d_s)/2$ on the surface. This is reasonable because ρ_c at $\theta=\theta_{\max}>\pi$, where $\cos\theta_{\max}=-(d_2-d_s)/(d_2+d_s)$ and the big-sphere center is at $x=x_q$, should be remarkably high and makes a significantly large, negative contribution to the force. Notice that the position of the local minimum is further apart from the step edge with increasing d_2. At $x=-L/2$, the negative component is smaller than the positive one due to the vanishing of ρ_c for $\pi<\theta<\theta_{\max}$. The net force becomes zero at a location (an x coordinate) smaller than $-L/2$ and larger than x_q. The presence of the negative regime followed by the positive regime leads to the positive

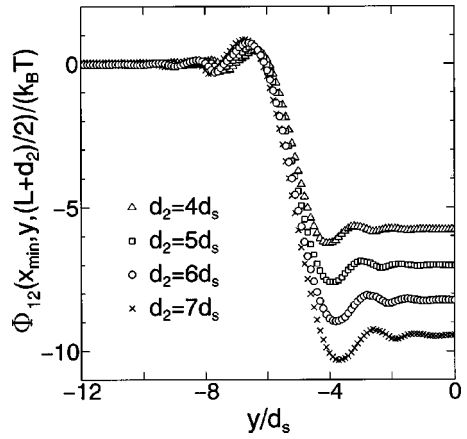

FIG. 10. The depletion potential Φ_{12} between solute 1 and solute 2 (the big sphere) along the trajectory of the big sphere: $x=x_{\min}=-L/2+\zeta$, $y\leqslant 0$, and $z=(L+d_2)/2$. It is scaled by k_BT and plotted for the four different values of d_2, $4d_s$, $5d_s$, $6d_s$, and $7d_s$. Since the potential is almost exactly symmetrical about $y=0$, the curves are shown only for $y\leqslant 0$. The step edge is located at $y=-L/2$ ($y/d_s=-5$).

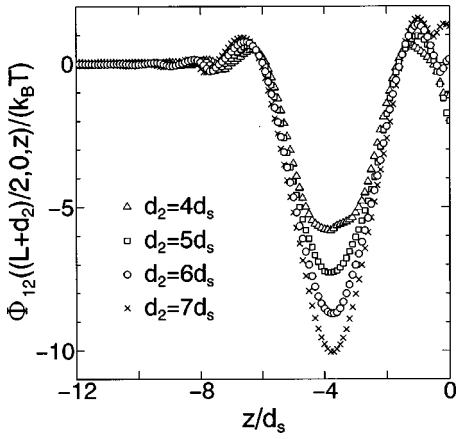

FIG. 11. The depletion potential Φ_{12} between solute 1 and solute 2 (the big sphere) along the trajectory of the big sphere: $x=(L+d_2)/2$, $y=0$, and $z\leqslant 0$. It is scaled by k_BT and plotted for the four different values of d_2, $4d_s$, $5d_s$, $6d_s$, and $7d_s$. Since the potential is exactly symmetrical about $z=0$, the curves are shown only for $z\leqslant 0$. The hemispherical cavity acts as a trench for $-d_1/2\leqslant z\leqslant d_1/2$ ($-2.5\leqslant z/d_s\leqslant 2.5$).

peak of the potential near the edge. As the big sphere moves further, the negative component does not significantly change, while the positive one decreases because of the vanishing of ρ_c occurring, with the result that at $x=x_0$ the net force becomes zero. Notice that x_0 is considerably smaller than $(-L+d_2)/2$. [At $x=x_0$, ρ_c in the vicinity of the corner for $x>x_0$ (i.e., on the right side) is higher than that for $x<x_0$ (i.e., on the left side) due to the geometric features of the corners.] Moreover, x_0 becomes deeper into the wall surface with increasing d_2. When the big sphere moves further, the positive regime is followed by a negative regime, leading to the shallow minimum of the potential. It is now obvious that values of the periodicity of the oscillations of g in Fig. 4 and Φ_{12} in Fig. 8 near the step edge are *not the same*. In contrast, the periodicity of the oscillations of $g(x,0,0)$ for $x\leqslant -(L+d_s)/2$ and $\Phi_{12}(x,0,0)$ for $x\leqslant -(L+d_2)/2$, for instance, is $\sim d_s$ regardless of d_2. As further information, the depletion potential $\Phi_{12}(x_{\min},y,(L+d_2)/2)$ $(x_{\min}=-L/2+\zeta)$ is shown for $y\leqslant 0$ in Fig. 10. $\Phi_{12}(x_{\min},y,(L+d_2)/2)$ also has a shallow minimum at $y\sim -L/2+\zeta$. The global maxima of $\Phi_{12}(x,y,(L+d_2)/2)$ occur at the four locations, $(x,y)\sim(-L/2+\zeta,-L/2+\zeta)$, $(L/2-\zeta,-L/2+\zeta)$, $(-L/2+\zeta,L/2-\zeta)$, and $(L/2-\zeta,L/2-\zeta)$.

Effects due to a trench can be studied by analyzing Φ_{12} along the trajectory of the big sphere, $x=(L+d_2)/2$, $y=0$, and $z\leqslant 0$, where the hemispherical cavity acts as a trench (see Fig. 11). When the big sphere protrudes over the trench, the overlap of the excluded regions decreases, so that the sphere is repelled from the edge. Though the detailed structure of the potential depends on the packing effects of the small spheres, it is observed in the figure that the sphere is *indeed repelled from the edge*. This trend is enhanced with increasing d_2.

D. Lock and key steric interaction between macromolecules

The solutes shown in Fig. 1 are treated with $d_2=3d_s$, $4d_s$, $5d_s$, and $6d_s$ and η_s is fixed at 0.367. The reduced density profiles of the small spheres, $g(x,0,0)$ for $x\geqslant(L-d_1+d_s)/2$ and $g((L+d_s)/2,0,z)$ for $z\geqslant 0$, are shown in Fig. 12. It is observed that the cavity is densely packed with the small spheres. A characteristic of $g(x,0,0)$ is that it does not exhibit simple oscillation with periodicity d_s and the third peak is higher than the second one, which indicates that the profile is largely influenced by the geometric feature of the cavity. The depletion potential, $\Phi_{12}(x,0,0)$ for $x>0$ shown in Fig. 13, gives useful information on the lock and key steric interaction between macromolecules. Stabilization occurs when the key is at contact with the lock: The stabilization free energies are $\sim -9.9k_BT$, $\sim -34k_BT$, $\sim -129k_BT$, and $\sim -20k_BT$ for $d_2=3d_s$, $4d_s$, $5d_s$, and $6d_s$, respectively. These values are much larger than those at contact with a flat surface, $\sim -4.2k_BT$, $\sim -5.3k_BT$, $\sim -6.4k_BT$, and $\sim -7.4k_BT$, respectively (see Fig. 8). The free energy for the key that exactly fits the lock is far larger than that for the other keys. For the key to contact the lock,

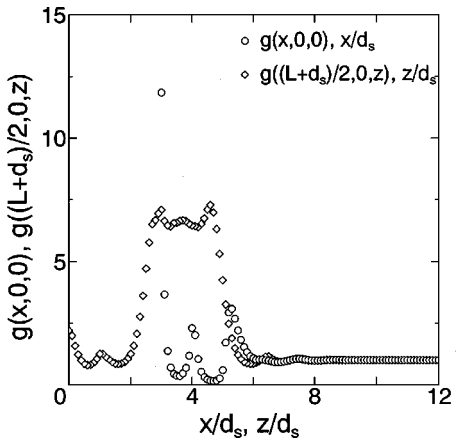

FIG. 12. The reduced density profiles of the small spheres, $g(x,0,0)$ for $x\geqslant(L-d_1+d_s)/2$ and $g((L+d_s)/2,0,z)$ for $z\geqslant 0$ (the latter is exactly symmetrical about $z=0$). Solute 1 is treated. The concave surface of the cavity is located at $x=(L-d_1)/2$ ($x/d_s=2.5$).

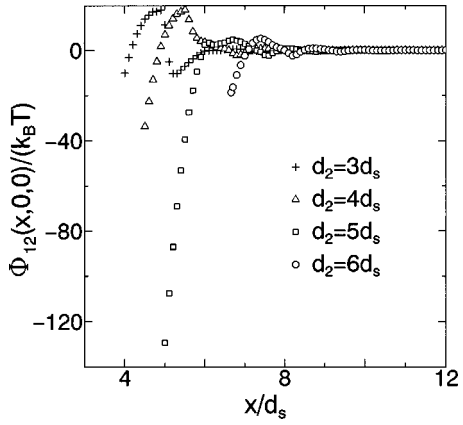

FIG. 13. The depletion potential Φ_{12} between solute 1 and solute 2 (the big sphere) along the trajectory of the big sphere: $x>0$, $y=0$, and $z=0$. It is scaled by k_BT and plotted for the four different values of d_2, $3d_s$, $4d_s$, $5d_s$, and $6d_s$. The concave surface of the cavity is located at $x=(L-d_1)/2$ ($x/d_s=2.5$). For $d_2=3d_s$, $4d_s$, and $5d_s$, the center of the key (big sphere) is located at $x=(L-d_1+d_2)/2$ when it is at contact with the lock (hemispherical cavity). For $d_2=6d_s$, however, the center is located at $x=L/2+\{(d_2/2)^2-(d_1/2)^2\}^{1/2}$. The key exactly fits the lock only for $d_2=5d_s$.

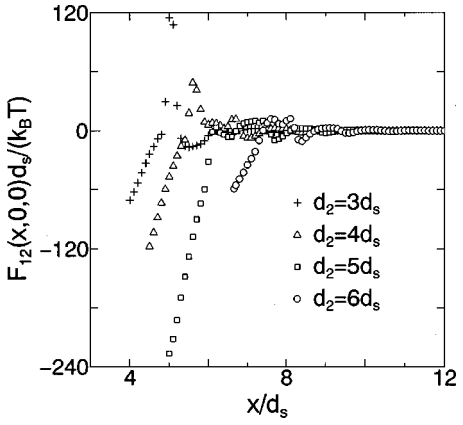

FIG. 14. The depletion force $F_{12}=-\partial\Phi_{12}/\partial x$ between solute 1 and solute 2 (the big sphere) along the trajectory of the big sphere: $x>0$, $y=0$, and $z=0$. The force is calculated by numerical differentiation of the potential plotted in Fig. 13.

it must overcome a free-energy barrier, taking the values of $\sim 27k_BT$, $\sim 20k_BT$, $\sim 7.0k_BT$, and $\sim 7.6k_BT$ for $d_2=3d_s$, $4d_s$, $5d_s$, and $6d_s$, respectively. It is obvious that the stabilization free energies and barriers are dependent on sizes of the lock and the key. In the cases of $d_2=2d_s$, $3d_s$, and $4d_s$ with $d_1=3d_s$, for example, the stabilization free energies are $\sim -10k_BT$, $\sim -49k_BT$, and $\sim -12k_BT$, respectively, and the barriers are $\sim 6.3k_BT$, $\sim 3.7k_BT$, and $\sim 3.4k_BT$, respectively. The barriers for the keys smaller than the lock are significantly higher than those for the other keys.

For $d_2=5d_s$, the volume of the excluded-region overlap occurring when the big sphere touches the cavity surface is estimated to be ~ 6 times larger than that in the case where the big sphere touches a flat surface. Nevertheless, the stabilization free energy in the former is ~ 20 times larger than that in the latter, which means a failure of the AO theory. The depletion force $F_{12}(x,0,0)=-\partial\Phi_{12}(x,0,0)/\partial x$ is calculated by numerical differentiation and plotted in Fig. 14. In contrast to the flat-wall case, when the key exactly fits the lock, even the contact density ρ_c in the vicinity of the corner makes an attractive contribution to the depletion force (the repulsive component is zero; see Fig. 15). Hence, the forces at and near contact predicted by the AO theory are underestimated simply by the factor $\rho_s/\rho_{c,\mathrm{av}}$ ($\rho_{c,\mathrm{av}}$ is the contact density averaged over the surface where its value does not vanish), which is seriously small, leading to the failure mentioned above. When the key with $d_2=6d_s$ is at contact with the lock, a tiny space within which the small spheres are packed remains, giving rise to high ρ_c and a significantly large, repulsive contribution to the force. Moreover, ρ_c in the vicinity of the corner makes a repulsive contribution. For these reasons, the attractive force at contact for the key with $d_2=6d_s$ is much smaller than that in the case of $d_2=5d_s$, leading to a smaller potential at contact (i.e., a smaller stabilization free energy).

As for one of the smaller keys with $d_2=3d_s$ and $4d_s$, at contact with the lock, the repulsive component is zero. However, ρ_c vanishes around a larger portion of the big sphere than in the case of $d_2=5d_s$ and nonzero ρ_c is lower due to the smaller value of d_2, leading to a smaller attractive component. As shown in Fig. 14, the force curve between one of these keys and the lock has a strongly repulsive peak at $x=x_p$. For $d_2=3d_s$, x_p equals $(L-d_1+d_2)/2+d_s$ that is exactly one solvent diameter away from the contact. For $d_2=4d_s$, x_p is slightly larger than $(L-d_1+d_2)/2+d_s$: $x_p\sim(L-d_1+d_2)/2+1.2d_s$. Here, as an example, solute 1 and the sphere of $d_2=4d_s$ fixed at $x=(L-d_1+d_2)/2+1.2d_s$ is regarded as a single solute and the reduced density profile $g(x,0,0)$ is calculated and plotted in Fig. 16. It is observed that the tiny space confined between the cavity and big-sphere surfaces is densely packed with the small spheres (see the closed circles in the figure). From a simple geometric consideration, one sees that ρ_c (ρ_c is symmetrical about $\theta=\pi$) for $\theta_r<\theta\leqslant\pi$, which yields a repulsive contribution to the force, is elevated. At $x\sim(L-d_1+d_2)/2+1.2d_s$, the repulsive contribution in the case of $d_2=4d_s$ with $\theta_r\sim 0.78\pi$ is much larger than that in the case of $d_2=5d_s$ with $\theta_r\sim 0.85\pi$. For $d_2=3d_s$, θ_r is 0.50π at $x\sim(L-d_1+d_2)/2+d_s$, leading to the exceptionally large, repulsive net force.

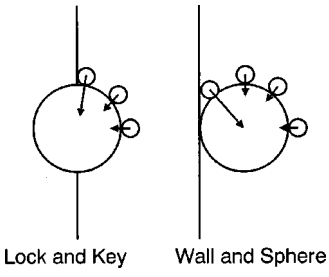

FIG. 15. Left: Forces acting on a big sphere (the key with $d_2=5d_s$) at contact with a cavity (the lock with $d_1=5d_s$). Forces originating from the contact density are represented by the arrows. A longer arrow corresponds to a stronger force. The big-sphere center is chosen as the origin and the contact density is expressed by $\rho_c(r=(d_2+d_s)/2,\theta)$ where θ is measured from the positive x axis. The contact density in the vicinity of the corner yields an attractive force while in the wall-sphere case (right) it does a repulsive one.

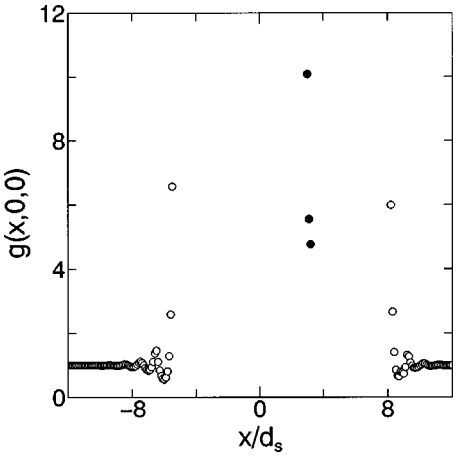

FIG. 16. The reduced density profile of the small spheres $g(x,0,(L+d_s)/2)$. Solute 1 and the sphere of $d_2=4d_s$ fixed at $x=(L-d_1+d_2)/2+1.2d_s$ is regarded as a single solute.

The presence of the strongly repulsive peak in the force curve for $d_2=3d_s$ and $4d_s$ makes the potential at contact considerably smaller. In summary, even when some keys of different sizes coexist, the key that exactly fits the lock is *exclusively* stabilized by the contact. The depletion effects are substantially large, and the selectivity given is much higher than one might expect from the overlap of the excluded regions and the AO theory.

IV. CONCLUSION

The author has employed the HNC equations solved on a 3D discrete cubic grid[18,19] to calculate the spatial distribution of the depletion potential between a big solute of arbitrary geometry and a big sphere immersed in small spheres forming the solvent. By analyzing the potential along a specific trajectory of the big sphere, effects due to the geometric feature of the big solute (e.g., step edges, trenches, corners, etc.) can be examined in detail. The potential along a surface with changing curvature can also be obtained. The 3D-HNC approach has been illustrated in two major analyses using solutes 1 and 2 shown in Fig. 1. One of them is for elucidating effects of the step edge on the lateral depletion potential, and the other is for simple model calculations of the lock and key steric interaction between macromolecules. The physical origins of the potentials obtained are discussed in detail by relating the corresponding forces to the contact density of the small spheres around the big sphere.

Along the trajectory considered for analyzing the step-edge effects, the big sphere moves at constant height, starting on the center of the wall surface and moving horizontally (in the negative direction along the x axis) past the edge. A potential minimum occurs not on the center but at a location much closer to the edge. The big sphere is repelled from the edge into the wall surface, and to escape to the bulk it must overcome a significantly high free-energy barrier. A positive peak occurs near the edge on the bulk side. These results are all in qualitatively good agreement with the experimental observation reported in Ref. 3. Since the AO theory can reproduce neither the potential minimum nor the positive peak, it underestimates the barrier. As far as the potential on the wall-surface center is concerned, however, the AO theory gives a fairly accurate value, implying that a cancellation of errors occurs as in the sphere-flat wall case (see Sec. III A). Effects of a trench on the lateral depletion potential are also briefly studied. When the big sphere protrudes over the trench, the depletion potential becomes significantly higher. It has thus been verified that a big sphere is repelled from the edge. This trend is enhanced with the increase in the big-sphere diameter.

A significant amount of information has been obtained from the model calculations for the lock–key interaction between macromolecules. The potential at contact (i.e., the stabilization free energy) for the key that exactly fits the lock ($d_2=5d_s$) is far larger than for smaller and larger keys and considerably in excess of the value predicted by the AO theory. For $d_2=5d_s$, the volume of the excluded-region overlap occurring when the big sphere touches the cavity surface (i.e., the key fits the lock) is estimated to be ~ 6 times larger than that in the case where the big sphere touches a flat surface. Nevertheless, the stabilization free energy in the former is ~ 20 times larger than in the latter. Since the AO theory is known to be accurate for the sphere–flat-wall case, the result implies a failure of the AO theory for the particular geometry. When the key exactly fits the lock, even the contact density in the vicinity of the corner makes an attractive contribution to the force. Moreover, there is no repulsive component, leading to an exceptionally strong, attractive net force. Hence, the forces at and near contact predicted by the AO theory are seriously underestimated with no cancellation of errors, leading to the failure mentioned above. Another significant result is that a very high free-energy barrier features the potential for a smaller key, preventing its access to the lock. Thus, the selectively given by the depletion effects is remarkably high. In the real biological systems, however, many other effects such as fluctuations of the macromolecular conformations as well as van der Waals, electrostatic, and hydrophobic forces will come into play. Still, the depletion forces should have substantially large influences on the lock–key interaction.

The author believes that the results presented are qualitatively correct and satisfactory even in a quantitative sense. To assure very high accuracy, however, the bridge functions must be included in the closure equations, and such refinement is to be pursued in future studies. It is not difficult to extend the present study to calculation of the potential between a pair of big solutes with arbitrary shapes that depends on the orientations of the solutes. Work in this direction is in progress.

ACKNOWLEDGMENTS

This work was supported by grants from the Japanese Ministry of Education, Science, Sports and Culture. The author thanks R. Roth, R. Evans, and S. Dietrich for sending him their DFT results, M. Yamamoto for providing him with a 3D-FFT program, and M. Ikeguchi for many useful comments on the numerical procedure. Acknowledgment is also due T. Oguni who was involved in an early stage of the present study.

[1] P. D. Kaplan, J. L. Rouke, A. G. Yodh, and D. J. Pine, Phys. Rev. Lett. **72**, 582 (1994).
[2] A. D. Dinsmore, A. G. Yodh, and D. J. Pine, Phys. Rev. E **52**, 4045 (1995).
[3] A. D. Dinsmore, A. G. Yodh, and D. J. Pine, Nature (London) **383**, 239 (1996).
[4] S. B. Zimmerman and A. P. Minton, Annu. Rev. Biophys. Biomol. Struct. **22**, 27 (1993).
[5] A. P. Minton, Curr. Opin. Biotechnol. **8**, 65 (1997).
[6] A. D. Dinsmore, D. T. Wong, P. Nelson, and A. G. Yodh, Phys. Rev. Lett. **80**, 409 (1998).
[7] S. Asakura and F. Oosawa, J. Chem. Phys. **22**, 1255 (1954).
[8] P. Attard, J. Chem. Phys. **91**, 3083 (1989).
[9] P. Attard and G. N. Patey, J. Chem. Phys. **92**, 4970 (1990).
[10] Y. Mao, M. E. Cates, and H. N. W. Lekkerkerker, Physica A **222**, 10 (1995).
[11] T. Biben, P. Bladon, and D. Frenkel, J. Phys.: Condens. Matter **8**, 10799 (1996).
[12] B. Götzelmann, R. Evans, and S. Dietrich, Phys. Rev. E **57**, 6785 (1998).
[13] R. Dickman, P. Attard, and V. Simonian, J. Chem. Phys. **107**, 205 (1997).
[14] R. Roth, B. Götzelmann, and S. Dietrich, Phys. Rev. Lett. **83**, 448 (1999).
[15] Y. Rosenfeld, Phys. Rev. Lett. **63**, 980 (1989).
[16] R. Roth, R. Evans, and S. Dietrich, Phys. Rev. E **62**, 5360 (2000).
[17] M. Kinoshita, S. Iba, K. Kuwamoto, and M. Harada, J. Chem. Phys. **105**, 7177 (1996).
[18] D. Beglov and B. Roux, J. Chem. Phys. **103**, 360 (1995).
[19] M. Ikeguchi and J. Doi, J. Chem. Phys. **103**, 5011 (1995).
[20] M. Kinoshita and T. Oguni, Chem. Phys. Lett. **351,** 79 (2002).